Geophysical Journal International

Geophys. J. Int. (2011) **187,** 63–74 doi: 10.1111/j.1365-246X.2011.05127.x

Three-dimensional adaptive higher order finite element simulation for geo-electromagnetics—a marine CSEM example

Christoph Schwarzbach,* Ralph-Uwe Börner and Klaus Spitzer

TU Bergakademie Freiberg, Institut für Geophysik, Gustav-Zeuner-Straße 12, 09596 *Freiberg, Germany. E-mail: cschwarz@eos.ubc.ca*

Accepted 2011 June 26. Received 2011 April 14; in original form 2010 September 8

SUMMARY

We present a new 3-D vector finite element code and demonstrate its strength by modelling a realistic marine CSEM scenario. Unstructured tetrahedral meshes easily allow for the inclusion of arbitrary seafloor bathymetry so that natural environments are mapped into the model in a close-to-reality way. A primary/secondary field approach, an adaptive mesh refinement strategy as well as a higher order polynomial finite element approximation improve the solution accuracy. A convergence study strongly indicates that the use of higher order finite elements is beneficial even if the solution is not globally smooth. The marine CSEM scenario also shows that seafloor topography gives an important response which needs to be reproduced by numerical modelling to avoid the misinterpretation of measurements.

Key words: numerical solutions; electromagnetic theory; marine electromagnetics.

1 INTRODUCTION

3-D modelling in geo-electromagnetics has been carried out for several decades (see, e.g. the review papers by Avdeev 2005; Börner 2010), starting predominantly with the integral equation method (Raiche 1974; Hohmann 1975; Weidelt 1975; Wannamaker *et al.* 1984; Newman *et al.* 1986; Wannamaker 1991; Xiong & Tripp 1997; Avdeev *et al.* 1997), followed by the finite difference method (Mackie *et al.* 1993; Newman & Alumbaugh 1995; Smith 1996; Streich 2009), and recently by the finite element method (Mogi 1996; Zunoubi *et al.* 1999; Zyserman & Santos 2000; Badea *et al.* 2001; Mitsuhata & Uchida 2004; Nam *et al.* 2007) and the finite volume method (Haber *et al.* 2000; Haber & Ascher 2001; Weiss & Constable 2006; Haber & Heldmann 2007). Amongst the different numerical methods the finite element method provides the greatest flexibility regarding model geometry, the option for a higher order spatial approximation and a rigorous framework for the treatment of virtually arbitrary constitutive parameter distributions. Consider as an example the presence of seafloor topography in a marine controlled source electromagnetics (CSEM) experiment. Bathymetric data can be incorporated into its model most naturally as a surface triangulation of the seafloor. To preserve the continuous nature of the surface triangulation the simulation volume needs to be tessellated by unstructured tetrahedral or hexahedral meshes. This suggests the use of the finite element method to discretize the boundary value problem underlying the simulation task. The finite difference method and its tensor product grids cannot preserve the surface triangulation but rather require that the surface is sampled and approximated in a staircase-like manner. Aiming at the development of an as most versatile as possible, state-of-the-art simulation code which provides geometric flexibility and high accuracy we implemented a new 3-D vector finite element code.

The use of a particular finite element type, the vector-valued Nédélec element (Nédélec 1980, 1986), has gradually become the established standard for discretizing the electric and magnetic field (Monk 2003) as the Nédélec element, other than the standard Lagrange element, reflects the continuity of the tangential field components and the discontinuity of the normal field component at parameter discontinuities. While Mogi (1996) still employed the scalar-valued Lagrange element, Zunoubi *et al.* (1999) and Nam *et al.* (2007) implemented the lowest order, that is, linear Nédélec element, also known as edge element (Jin 1993). Zyserman & Santos (2000) followed a significantly different, domain decomposition approach including a locally higher order polynomial approximation. These implementations, as ours presented here, discretize the electric or magnetic field. Badea *et al.* (2001) and Mitsuhata & Uchida (2004) decompose the fields in terms of vector and scalar potentials. Their benefit of solving for a smoother potential field and obtaining a simpler or reduced set of equations is somewhat weakened by having to carry out numerical differentiation to compute the fields. Since the electric field is oftentimes the measured quantity we give preference to the direct formulation in terms of the electric field.

Our finite element code combines a list of features which, so far, could only been found in commercial software packages like COMSOL Multiphysics®. Their use might be useful for a wealth of problems (e.g. Börner *et al.* 2008) but involves all disadvantages of using a black-box solver. Building on and extending existing libraries we have implemented a new finite element software which features unstructured tetrahedral meshes, higher order polynomial

*Now at: University of British Columbia, Department of Earth and Ocean Sciences, 6339 Stores Road, Vancouver, BC, V6T 1Z4, Canada.

approximations and adaptive mesh refinement. The software is tailored but not restricted to geophysical applications. Section 2 of this paper will give some theoretical background and implementation details. In Section 3, we present numerical examples which illustrate our software's features. Firstly, a convergence study provides some numerical evidence that the use of higher order polynomials might be beneficial even if the solution is not globally smooth. Secondly, the geometric flexibility of unstructured tetrahedral meshes is demonstrated by inclusion of seafloor topography into our model. Finally, we present a comparative study on the canonical disc model (Weiss & Constable 2006) and its extension by an air halfspace.

2 METHOD

Electromagnetic phenomena are mathematically described by the system of Maxwell's equations. We consider the time-harmonic case of an electric dipole oscillating at a single frequency and therefore assume an $\exp(-i\omega t)$ time dependency throughout the following. The symbol i denotes the imaginary unit, ω angular frequency and t time.

2.1 Boundary value problem

We solve the vector Helmholtz equation in terms of the secondary electric field $\boldsymbol{E}_s$

$$\begin{aligned}&\operatorname{curl}\left(\mu^{-1}\operatorname{curl}\boldsymbol{E}_s\right) - i\omega(\sigma - i\omega\varepsilon)\boldsymbol{E}_s \\ &\quad = \operatorname{curl}\left(\left[\mu_p^{-1} - \mu^{-1}\right]\operatorname{curl}\boldsymbol{E}_p\right) - i\omega([\sigma_p - \sigma] - i\omega[\varepsilon_p - \varepsilon])\boldsymbol{E}_p\end{aligned} \tag{1a}$$

within the domain Ω subject to a homogeneous Dirichlet boundary condition

$$\boldsymbol{n} \times \boldsymbol{E}_s = \boldsymbol{0} \tag{1b}$$

on the domain boundary $\partial\Omega$. μ, σ and ε denote magnetic permeability, electrical conductivity and electric permittivity, respectively. $\boldsymbol{E}_p$ is the primary electric field which solves Maxwell's equations with constitutive parameters $\mu_p, \sigma_p, \varepsilon_p$. $\boldsymbol{n}$ denotes the outer unit normal vector on the boundary. We consider here only the simple case of a homogeneous Dirichlet boundary condition to reduce complexity of notation and to accommodate for the numerical examples of Section 3. However, the method and implementation are not restricted to that case. A more general setting is given in Schwarzbach (2009).

Taking the L_2-inner product of the partial differential equation (1a) with a vector test function $\boldsymbol{\Phi}$ and carrying out partial integration we obtain the variational form of boundary value problem (1) (Monk 2003): search $\boldsymbol{E}_s \in \mathcal{U}$ such that

$$\begin{aligned}&\int_\Omega \operatorname{curl}\overline{\boldsymbol{\Phi}} \cdot \left(\mu^{-1}\operatorname{curl}\boldsymbol{E}_s\right)\, d^3r - i\omega \int_\Omega \overline{\boldsymbol{\Phi}} \cdot ((\sigma - i\omega\varepsilon)\boldsymbol{E}_s)\, d^3r \\ &\quad = \int_\Omega \operatorname{curl}\overline{\boldsymbol{\Phi}} \cdot \left(\left[\mu_p^{-1} - \mu^{-1}\right]\operatorname{curl}\boldsymbol{E}_p\right)\, d^3r \\ &\qquad - i\omega \int_\Omega \overline{\boldsymbol{\Phi}} \cdot (([\sigma_p - \sigma] - i\omega[\varepsilon_p - \varepsilon])\boldsymbol{E}_p)\, d^3r\end{aligned} \tag{2a}$$

for all $\boldsymbol{\Phi} \in \mathcal{U}$. The space of test and trial functions is defined by

$$\mathcal{U} = \{\boldsymbol{E} \in H_{\text{curl}}(\Omega) : \boldsymbol{n} \times \boldsymbol{E} = \boldsymbol{0} \text{ on } \partial\Omega\} \tag{2b}$$

where

$$H_{\text{curl}}(\Omega) = \left\{\boldsymbol{E} \in (L_2(\Omega))^3 : \operatorname{curl}\boldsymbol{E} \in (L_2(\Omega))^3\right\} \tag{2c}$$

is the space of functions with a well-defined curl and $L_2(\Omega)$ is the space of square integrable functions on Ω. The notation $\overline{\boldsymbol{\Phi}}$ denotes the complex conjugate of $\boldsymbol{\Phi}$.

2.2 Finite element solution

The variational problem (2) is the point of departure for the numerical solution of the boundary value problem (1) using the finite element method. For a comprehensive introduction to the finite element method the reader is referred to standard textbooks like, for example, Jin (1993) and Monk (2003). We will only give a brief outline here and review some details which are essential for the understanding of our numerical experiments.

The finite element discretization of the variational problem proceeds as follows. Firstly, the domain Ω is tessellated by tetrahedra (see Fig. 3 in Section 3 for an example). Secondly, the infinite dimensional function space $\mathcal{U}$ in (2) is replaced by a finite dimensional function space $\mathcal{U}_h$. $\mathcal{U}_h$ consists of vector functions which are componentwise polynomials of degree up to p within each tetrahedron and which vanish on all but a few tetrahedra. The vector functions' tangential components are continuous across the interface between two adjacent tetrahedra. Note, however, that no assumptions are made concerning the normal component which can be discontinuous at the interface. Next, a finite set of basis functions $\{\boldsymbol{\Phi}_i\}_{i=1}^n$ can be constructed such that it spans $\mathcal{U}_h$. Instead of seeking a solution $\boldsymbol{E}_s \in \mathcal{U}$ we attempt to find an approximate solution $\tilde{\boldsymbol{E}}_s \in \mathcal{U}_h$ such that (2a) holds for all test functions $\boldsymbol{\Phi}_i, i = 1, \ldots, n$. Expanding $\tilde{\boldsymbol{E}}_s$ in terms of the basis functions

$$\tilde{\boldsymbol{E}}_s = \sum_{j=1}^{n} e_j \boldsymbol{\Phi}_j \tag{3}$$

produces a system of linear equations

$$\boldsymbol{A}\boldsymbol{e} = \boldsymbol{f}, \tag{4a}$$

where $\boldsymbol{A} \in \mathbb{C}^{n\times n}$, $\boldsymbol{e}, \boldsymbol{f} \in \mathbb{C}^n$ with components

$$\begin{aligned}A_{i,j} &= \int_\Omega \operatorname{curl}\overline{\boldsymbol{\Phi}_i} \cdot \left(\mu^{-1}\operatorname{curl}\boldsymbol{\Phi}_j\right)\, d^3r \\ &\quad - i\omega \int_\Omega \overline{\boldsymbol{\Phi}_i} \cdot ((\sigma - i\omega\varepsilon)\boldsymbol{\Phi}_j)\, d^3r\end{aligned} \tag{4b}$$

$$\begin{aligned}f_i &= \int_\Omega \operatorname{curl}\overline{\boldsymbol{\Phi}_i} \cdot \left(\left[\mu_p^{-1} - \mu^{-1}\right]\operatorname{curl}\boldsymbol{E}_p\right)\, d^3r \\ &\quad - i\omega \int_\Omega \overline{\boldsymbol{\Phi}_i} \cdot (([\sigma_p - \sigma] - i\omega[\varepsilon_p - \varepsilon])\boldsymbol{E}_p)\, d^3r.\end{aligned} \tag{4c}$$

In practice, the basis functions $\boldsymbol{\Phi}_i$ are real-valued. Therefore, the matrix $\boldsymbol{A}$ is symmetric, $\boldsymbol{A} = \boldsymbol{A}^T$, but not Hermitian. Since the finite element basis functions have small support the matrix $\boldsymbol{A}$ is sparse. Furthermore, one can show that $\boldsymbol{A}$ is indefinite (e.g. Monk 2003).

The vector $\boldsymbol{e}$ contains the finite element basis function expansion coefficients e_j from (3) which are called degrees of freedom (dofs). They are defined more precisely by a set of linear functionals $\{\mathcal{A}_i\}_{i=1}^n$ which map functions $\tilde{\boldsymbol{E}}_s \in \mathcal{U}_h$ onto the vector space $\mathbb{C}^n$. As an example, consider the lowest order Nédélec/edge element with pointwise dofs. The dofs are defined as the tangential field component at the midpoint $\boldsymbol{x}_i$ of an edge, multiplied by the edge length. Let $\boldsymbol{t}_i$ be the tangential vector of edge i with length $\|\boldsymbol{t}_i\|$. Then, $\mathcal{A}_i(\tilde{\boldsymbol{E}}_s) := \boldsymbol{t}_i \cdot \tilde{\boldsymbol{E}}_s(\boldsymbol{x}_i)$.

The linear functionals $\mathcal{A}_i$ can also be applied to an arbitrary function $\boldsymbol{E}_s \in \mathcal{U}$. Then, the function $\Pi\boldsymbol{E}_s := \sum_{i=1}^n \mathcal{A}_i(\boldsymbol{E}_s)\boldsymbol{\Phi}_i$ defines a projection of $\boldsymbol{E}_s$ onto $\mathcal{U}_h$ under projection operator Π.

Note that for $\tilde{\boldsymbol{E}}_s \in \mathcal{U}_h$, Π is the identity operator, $\Pi\tilde{\boldsymbol{E}}_s = \tilde{\boldsymbol{E}}_s$, and $\mathcal{A}_i(\tilde{\boldsymbol{E}}_s) = e_i$. In general, $\boldsymbol{E}_s \in \mathcal{U}$ leaves $\|\boldsymbol{E}_s - \Pi\boldsymbol{E}_s\| \neq 0$.

The set of linear functionals $\mathcal{A}_i$, $i = 1, \ldots, n$, spans the so-called dual space $\mathcal{U}_h^*$ of $\mathcal{U}_h$. $\mathcal{U}_h^*$ is equipped with the discrete ℓ_2-norm

$$\|\boldsymbol{E}_s\|_{\ell_2} = \left(\sum_{i=1}^{n} \overline{\mathcal{A}_i(\boldsymbol{E}_s)}\mathcal{A}_i(\boldsymbol{E}_s)\right)^{1/2} \tag{5}$$

corresponding to the continuous L_2-norm defined in the Hilbert space $\mathcal{U}_h$

$$\|\boldsymbol{E}_s\|_{L_2(\Omega)} = \left(\int_\Omega \overline{\boldsymbol{E}_s} \cdot \boldsymbol{E}_s \, d^3r\right)^{1/2}. \tag{6}$$

These norms will be required to quantify the solution error in Section 3.

2.3 Implementation

Assembly of the system of linear equations (4), its solution and post-processing steps like the evaluation of the solution according to (3) and its derivatives at arbitrary points in Ω have been implemented in a C++ software package. Our implementation is based on and extends the finite element library FEMSTER (Castillo *et al.* 2005). Even though we only consider isotropic and piecewise constant constitutive parameters in this paper, the implementation includes anisotropic and piecewise polynomial parameters as well as a set of transformed constitutive parameters which define a perfectly matched layer (PML, Berenger 1994; after Monk 2003). The constitutive parameters form part of the integrals in (4b) and (4c) which are evaluated numerically using appropriate quadrature rules. The system of linear equations is solved directly using PARDISO (Schenk & Gärtner 2004, 2006) or iteratively using the quasi-minimum residual method (QMR, Freund & Nachtigal 1994). As a prerequisite for the finite element assembly and solution the computational domain needs to be tessellated. We employ the tetrahedral mesh generator TETGEN (Si 2007).

2.4 Adaptive mesh refinement

Ad hoc construction of a mesh tailored to the solution and providing a solution of sufficient quality is difficult. Therefore, an automated, iterative mesh generation procedure has been implemented. Starting from a coarse initial mesh which just takes into account the model geometry, a sequence of meshes is constructed such that the mesh is locally refined where the solution error is largest. The *a posteriori* error indicator of Beck & Hiptmair (1999) is used to estimate the solution error. Given the finite element approximation of the electric field $\tilde{\boldsymbol{E}}_s$ an approximation of the magnetic field can be derived in two different ways. First, we apply Faraday's law directly and obtain

$$\tilde{\boldsymbol{H}}_s = (i\omega\mu)^{-1}\,\mathrm{curl}\,\tilde{\boldsymbol{E}}_s = (i\omega\mu)^{-1}\sum_{j=1}^{n} e_j \mathrm{curl}\boldsymbol{\Phi}_j. \tag{7}$$

By construction the tangential components of $\tilde{\boldsymbol{E}}_s$ are continuous across element interfaces and so is the normal component of the magnetic flux $\tilde{\boldsymbol{B}}_s = (i\omega)^{-1}\mathrm{curl}\tilde{\boldsymbol{E}}_s$. The finite element spaces do not impose continuity of the tangential component of $\tilde{\boldsymbol{B}}_s$. Consequently, the magnetic field computed according to eq. (7) does not satisfy exactly the proper physical interface conditions even if μ is constant. Note, however, that continuity of the tangential magnetic field components is satisfied approximately because this condition is contained in the variational formulation (2).

The second magnetic field approximation seeks a magnetic field $\hat{\boldsymbol{H}}_s$ that satisfies exactly the continuity of its tangential components. This is achieved by applying the finite element method to eq. (7) and computing $\hat{\boldsymbol{H}}_s$ as the L_2-projection of $(i\omega\mu)^{-1}\,\mathrm{curl}\,\tilde{\boldsymbol{E}}_s$ onto $\mathcal{V}_h$. $\mathcal{V}_h$ is a finite element subspace of $H_{\mathrm{curl}}(\Omega)$ similar to $\mathcal{U}_h \subset \mathcal{U}$ except that we do not exclude functions with $\boldsymbol{n} \times \hat{\boldsymbol{H}}_s = \boldsymbol{0}$. The resulting system of linear equations is about as large as the original problem but much easier to solve since only a real, symmetric positive definite mass matrix needs to be inverted. Inspired by the definition of magnetic field energy, a weighted norm of the difference between the two magnetic field approximations $\hat{\boldsymbol{H}}_s$ and $\tilde{\boldsymbol{H}}_s$

$$\eta_{K_i} = \int_{K_i} \overline{\left(\hat{\boldsymbol{H}}_s - \tilde{\boldsymbol{H}}_s\right)} \cdot \mu \left(\hat{\boldsymbol{H}}_s - \tilde{\boldsymbol{H}}_s\right) d^3r \tag{8}$$

is computed and serves as a local error indicator for element K_i. Assume that there are m elements which are enumerated such that $\eta_{K_1} \geq \eta_{K_2} \geq \ldots \geq \eta_{K_m}$. Then, element K_i is selected for refinement if $\eta_{K_i} \geq \alpha_1\eta_{K_1}$ or $i \leq \alpha_2 m$. The parameters α_1 and α_2 control the refinement process. The values $\alpha_1 = 0.1$ and $\alpha_2 = 0.001$ have been used for the numerical examples in the following section.

3 NUMERICAL EXAMPLES

We present three numerical examples which illustrate the validity of our code, demonstrate the benefit of using a higher order polynomial approximation, and show the capability for modelling complicated geometries, here, seafloor topography. To isolate the effects of mesh size, polynomial degree and seafloor topography, the first two example models are variations of a very compact, basic marine scenario which consists just of two halfspaces filled with seawater and seabed sediments. The third example incorporates some features required in a more realistic marine CSEM scenario such as the air halfspace (Constable & Weiss 2006; Weidelt 2007) and large transmitter/receiver separations.

Since the first two examples build on some common model features we detail them here. The computational volume is $\Omega = \{(x, y, z) : -2\,\mathrm{km} \leq x, y \leq 2\,\mathrm{km}, -1.5\,\mathrm{km} \leq z \leq 2.5\,\mathrm{km}\}$ and divided into two subdomains representing seawater and seabed. Electrical conductivity is $3.3\,\mathrm{S\,m^{-1}}$ for the seawater and $1\,\mathrm{S\,m^{-1}}$ for the seabed sediments. An x-directed electric dipole radiating with frequency 1 Hz is placed 100 m above the seafloor at $x = y = 0$ and $z = -100\,\mathrm{m}$. The primary field $\boldsymbol{E}_p$ in eq. (1) is chosen to be the electric field of an electric dipole placed within a homogeneous fullspace filled with seawater. Sources for the secondary field are consequently caused by the difference in electrical conductivity and restricted to the seabed.

3.1 Convergence study

The first numerical experiment has been set up to validate our code by comparison to a known solution and to examine the potential benefit of using higher order polynomials. In order to be able to compute an exact solution we consider a planar interface between seawater and seabed. We call this model the flat seafloor model. The solution of a horizontal electric dipole in a two-layered medium can be computed analytically and expressed in form of Hankel integrals (Sommerfeld 1964). The Hankel integrals are evaluated numerically using the digital filter algorithm of Anderson (1989).

The numerical solution has been computed on a sequence of adaptively refined meshes. Starting from the same coarse mesh comprising 16 464 tetrahedra, three sequences have been created

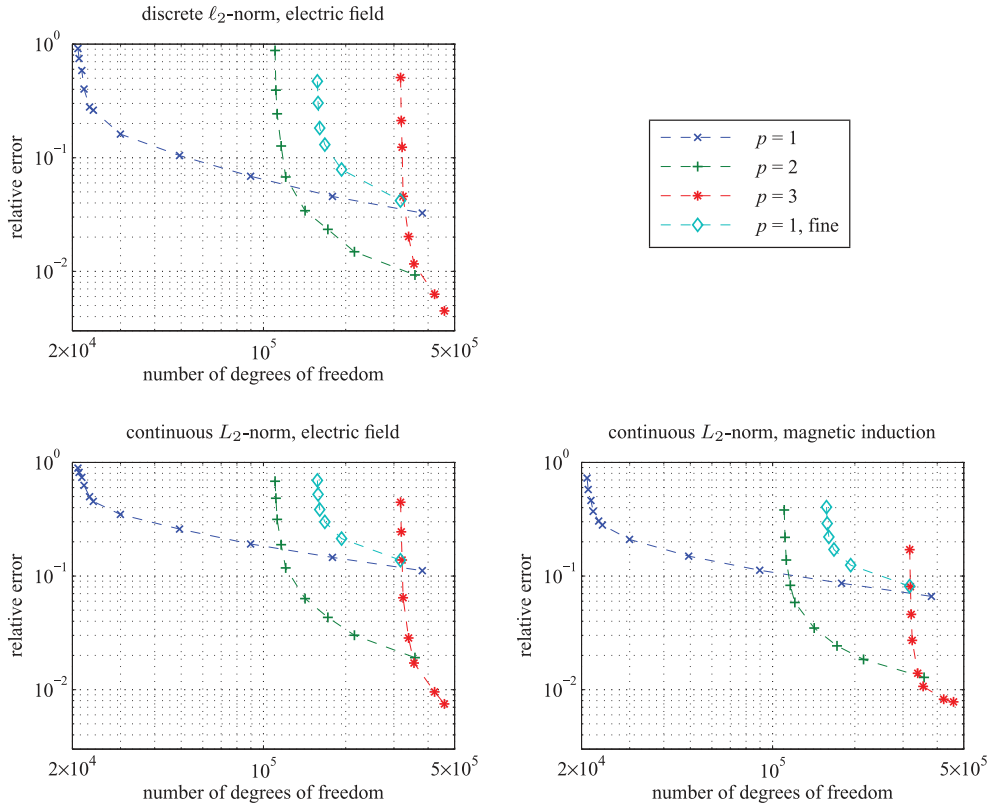

Figure 1. Various global relative error measures as a function of the number of unknowns of a sequence of adaptively refined meshes. Polynomial degrees $p = 1, 2, 3$ for coarse initial mesh and $p = 1$ for finer initial mesh.

using a finite element basis with polynomial degrees $p = 1, 2, 3$. Using a higher order polynomial on the same mesh can be considered a kind of global mesh refinement (p-refinement). To see the effect of its counterpart, h-refinement, we generate another sequence of meshes with $p = 1$ starting from a finer initial mesh of 130 025 tetrahedra. The adaptive refinement procedure was stopped before the number of dofs exceeded half a million. The evolution of the number of dofs can be seen in any of the three subplots of Fig. 1 by following the trace of the four differently coloured curves on the abscissa. The main focus of the figure, though, is the summary of the relative error for each of the four mesh sequences. We consider three different error quantities.

The discrete ℓ_2-norm error of the electric field

$$\|\tilde{\boldsymbol{E}}_s - \boldsymbol{E}_s\|_{\ell_2} = \left(\sum_{i=1}^{n} \overline{(e_i - \mathcal{A}_i(\boldsymbol{E}_s))} (e_i - \mathcal{A}_i(\boldsymbol{E}_s)) \right)^{1/2} \tag{9}$$

is derived from (5) by invoking the linearity of the dofs $\mathcal{A}_i$ and the identity $e_i = \mathcal{A}_i(\tilde{\boldsymbol{E}}_s)$. Normalization by the discrete ℓ_2-norm of the true solution gives the relative error $\|\tilde{\boldsymbol{E}}_s - \boldsymbol{E}_s\|_{\ell_2} / \|\boldsymbol{E}_s\|_{\ell_2}$ which is plotted in the top left panel of Fig. 1. This measure only involves the dofs and provides the most direct view on the error of the discrete solution. Note that in particular for the case of the piecewise linear approximation ($p = 1$) only one field component, the projection of the field onto each edge at the edge's midpoint, is compared to the true solution at one and the same spatial location. The discrete ℓ_2-norm does not involve any interpolation, in contrast to the two following error quantities employing the continuous Hilbert space L_2-norm (6).

The L_2-norm involves integration over the entire domain and consequently requires interpolation of the discrete solution, the dofs, to any point in Ω according to eq. (3). This norm gives rise to the absolute L_2-norm error of the electric field

$$\|\tilde{\boldsymbol{E}}_s - \boldsymbol{E}_s\|_{L_2(\Omega)} = \left(\int_\Omega \overline{(\tilde{\boldsymbol{E}}_s - \boldsymbol{E}_s)} \cdot (\tilde{\boldsymbol{E}}_s - \boldsymbol{E}_s)\, d^3r \right)^{1/2}. \tag{10}$$

Normalization by the continuous L_2-norm of the true solution produces the relative error $\|\tilde{\boldsymbol{E}}_s - \boldsymbol{E}_s\|_{L_2(\Omega)} / \|\boldsymbol{E}_s\|_{L_2(\Omega)}$ which is depicted in the lower left panel of Fig. 1.

By applying Faraday's law to the numerical solution, we also obtain the absolute L_2-norm error of the magnetic induction

$$\|\tilde{\boldsymbol{B}}_s - \boldsymbol{B}_s\|_{L_2(\Omega)} = \left(\int_\Omega \overline{(i\omega \operatorname{curl} \tilde{\boldsymbol{E}}_s - \boldsymbol{B}_s)} \cdot (i\omega \operatorname{curl} \tilde{\boldsymbol{E}}_s - \boldsymbol{B}_s)\, d^3r \right)^{1/2} \tag{11}$$

Note that there is no corresponding discrete measure since the derivative of the numerical solution is carried out on the finite element basis functions $\boldsymbol{\Phi}_j$ involving the same linear coefficients e_j. Normalization by the continuous L_2-norm of the true solution yields the relative error $\|\tilde{\boldsymbol{B}}_s - \boldsymbol{B}_s\|_{L_2(\Omega)} / \|\boldsymbol{B}_s\|_{L_2(\Omega)}$ which is shown in the lower right panel of Fig. 1.

All three quantities give a similar picture of the evolution of the solution error as the mesh is locally refined. First, only few dofs need to be added to reduce the error rapidly. In this stage, the largest discretization errors are concentrated around the centre of the secondary source, where the field values and gradients are largest. They are accommodated for by a very focussed mesh refinement. Subsequently, the error distribution becomes smoother and more elements are involved in the refinement process. The number of dofs consequently grows faster at this stage.

At the finest mesh level, the piecewise cubic approximation produces the most accurate solution, the piecewise quadratic approximation the next accurate solution and the piecewise linear approximations the least accurate solution. The difference between $p = 1$ and $p = 2$ is more pronounced than between $p = 2$ and $p = 3$. For $p = 1$, the accuracy obtained within the limit of half a million dofs is about the same for both the coarse and the fine starting mesh. We conclude that a coarse starting mesh suffices for the error indicator to guide the mesh refinement process such that the overall error is reduced properly. The coarse starting mesh is more efficient than a finer starting mesh as dofs are only added where needed. Furthermore, the higher order polynomial approximation seems to be highly beneficial. In practice, however, the use of higher order finite elements might be limited when complex geometries give rise to rather large meshes and a too large number of dofs even for the initial mesh. The bathymetry model of the following section gives an example where only $p = 2$ proves to be computationally tractable while $p = 3$ is intractable.

Table 1. Mesh statistics. Number of elements and degrees of freedom (dofs) for each refinement level and piecewise linear $p = 1$ finite element basis functions. Piecewise quadratic $p = 2$ basis functions are only used for the last mesh level.

Flat seafloor model			Bathymetry model		
Level	Elements	dofs	Level	Elements	dofs
		$p = 1$			
1	16 545	21 016	1	380 809	447 492
2	16 717	21 216	2	382 193	449 082
3	16 937	21 472	3	390 848	459 043
4	17 499	22 124	4	416 553	488 660
5	19 281	24 181	5	468 680	548 778
6	21 292	26 509	6	542 425	633 820
7	30 892	37 610			
8	55 383	65 875			
9	118 793	139 063			
		$p = 2$			
9	118 793	755 762	6	542 425	3 444 676

3.2 Seafloor topography

Our second numerical example is constructed from a synthetic topography data set provided by the INRIA Gamma team (2008). The bathymetry is depicted in Fig. 2 and the derived model called the bathymetry model. To quantify the accuracy of the solution and to qualitatively estimate the distortion of the electromagnetic field by the seafloor topography, the flat seafloor model from the previous section is considered for comparison. Both models have been spatially discretized using the adaptive mesh refinement strategy. The mesh hierarchies are listed in Table 1. To reduce the additional computational cost of the adaptive mesh refinement procedure, the solution of the boundary value problem for the initial and intermediate mesh levels is solved using a piecewise linear approximation ($p = 1$). Only the final solution is computed with piecewise quadratic finite element basis functions ($p = 2$). The number of electric field dofs is also given in Table 1. The linear equation systems of the mesh generation phase ($p = 1$) where solved directly using PARDISO, those of the production runs ($p = 2$) iteratively using QMR. While the number of 3 444 676 dofs for the bathymetry model production run with $p = 2$ were still tractable, $p = 3$ would have required the solution of a system with 12 503 729 unknowns and was considered intractable.

The considerably larger number of elements in the initial mesh of the bathymetry model is a consequence of the relatively dense surface triangulation of the bathymetry data set with a regular grid spacing of 250 m in x- and y-direction. This can be seen by comparing the initial meshes of both the flat seafloor and the bathymetry model in the top row of Fig. 3. During the refinement process, the mesh is refined directly beneath the primary source at the seafloor where the secondary sources and, consequently, the secondary field assumes its maximum magnitude. The final meshes of both models are shown in the bottom row of Fig. 3. The smallest edge lengths of the final meshes, 7.6 m for the flat seafloor model and 5.5 m for the bathymetry model, are comparable.

To illustrate the spatial distribution of the solution error, we compute the L_2-norm error of the electric and magnetic field elementwise. In contrast to the global measures (10) and (11) of the previous section, the relative error here is computed separately for each element K_i by integrating the norm $\|\cdot\|$ just over the ith tetrahedron. The elementwise relative errors of the electric field $\delta\{\tilde{\boldsymbol{E}}_s\} = \|\tilde{\boldsymbol{E}}_s - \boldsymbol{E}_s\|_{L_2(K_i)}/\|\boldsymbol{E}_s\|_{L_2(K_i)}$ and of the magnetic field $\delta\{\tilde{\boldsymbol{H}}_s\} = \|\tilde{\boldsymbol{H}}_s - \boldsymbol{H}_s\|_{L_2(K_i)}/\|\boldsymbol{H}_s\|_{L_2(K_i)}$ are plotted in the top row of Fig. 4. The relative error of the numerically computed secondary fields within the smaller portion of the computational volume shown is mostly less than 1 per cent. The relative error of the magnetic field contains pronounced regions where it is significantly larger. This is an artefact of the relative measure used since the magnetic field has a pronounced minimum which exactly coincides with the maximum of the relative error. This can be seen by comparing the top row of Fig. 4 with the bottom row where the elementwise L_2-norm of the fields, $\|\boldsymbol{E}_s\|_{L_2(K_i)}$ and $\|\boldsymbol{H}_s\|_{L_2(K_i)}$, are shown.

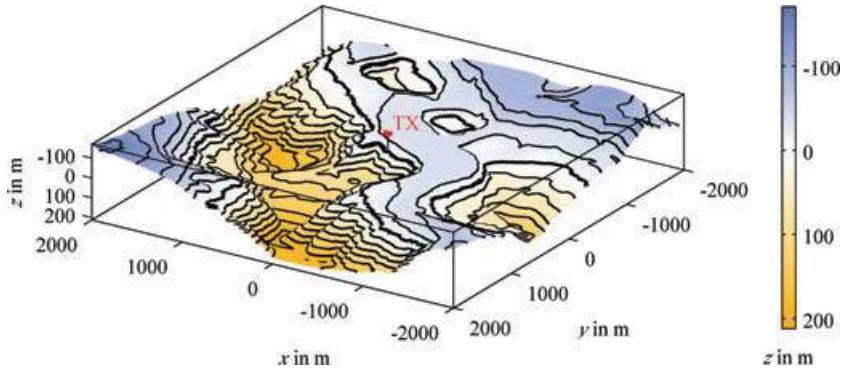

Figure 2. Seafloor bathymetry, 2× vertical exaggeration. An x-directed electric dipole TX is placed 100 m above the seafloor.

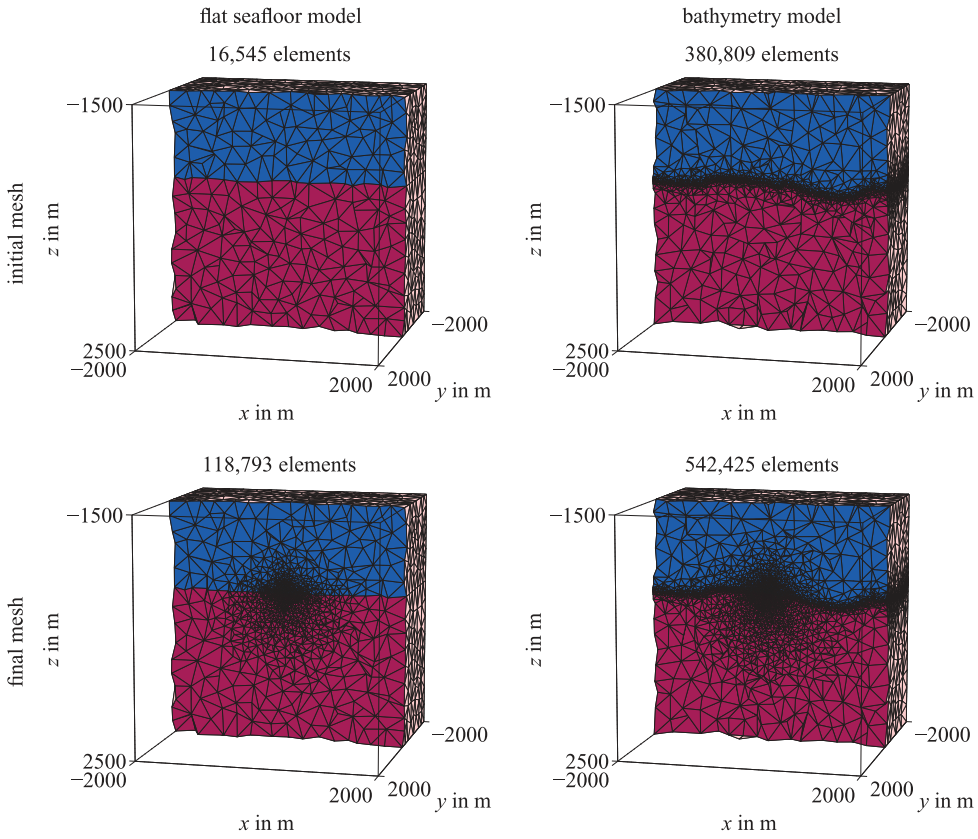

Figure 3. Slice through the initial and final tetrahedral meshes of the flat seafloor (left-hand side) and the bathymetry model (right-hand side).

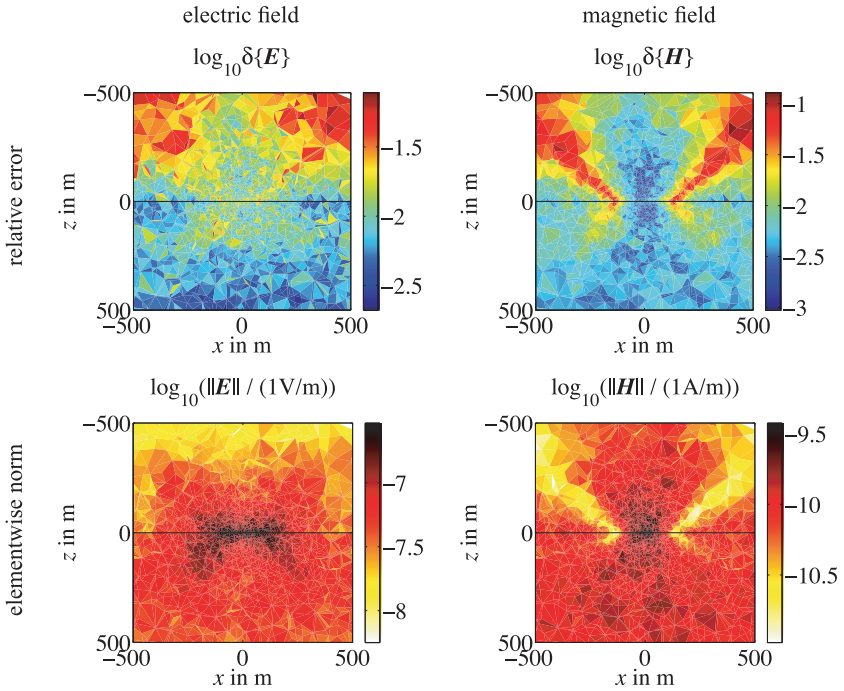

Figure 4. Flat seafloor model. Relative error of the electric and magnetic field in the x–z plane at $y = 0$ (top row). Compare the pattern of the relative error with the elementwise L_2-norm of $\boldsymbol{E}$ and $\boldsymbol{H}$ (bottom row) which has been used to normalize the absolute error.

Fig. 5 shows the non-vanishing secondary electric and magnetic field components for the flat seafloor model within the x–z plane through the dipole source at $y = 0$. The top row insets show the absolute value of the complex valued field components, the bottom row insets the phase. Due to the 1-D earth model geometry the fields exhibit a symmetric pattern. The H_x, E_y and H_z components vanish within this plane. If bathymetry is added to the model, the symmetries are disturbed and all field components assume

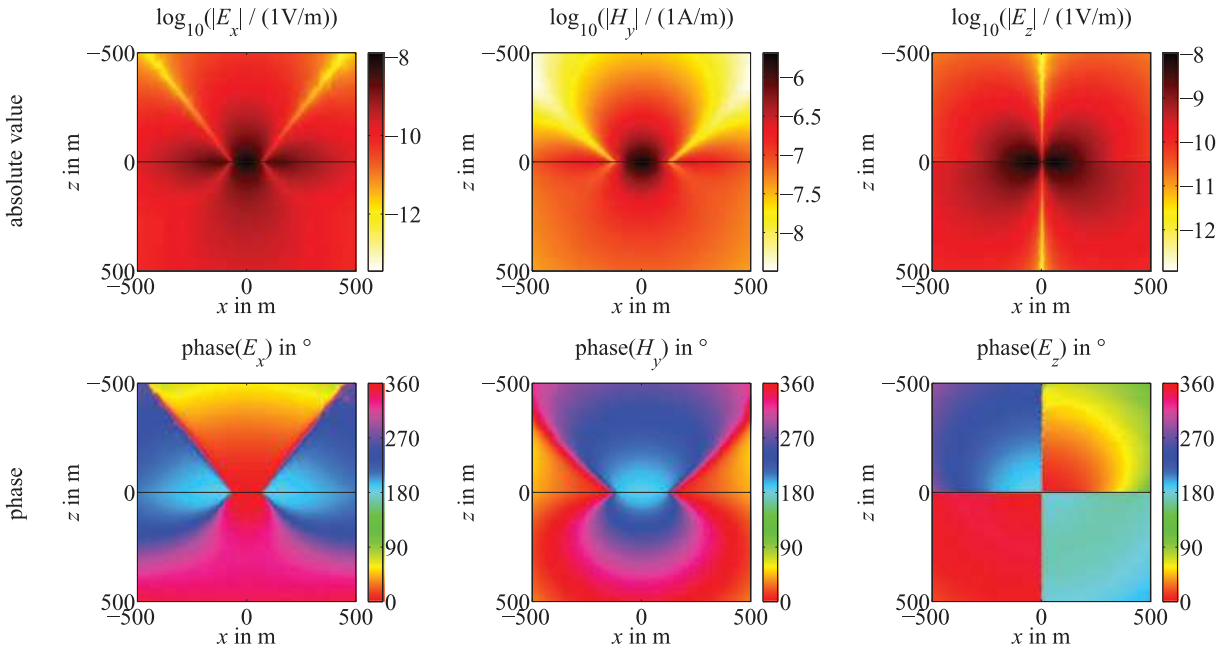

Figure 5. Flat seafloor model. Non-vanishing secondary field components in the x–z plane at $y = 0$. Absolute value and phase of the complex vector components.

non-zero values. This can be seen from Fig. 6 which shows all three field components of the secondary electric and magnetic field.

For a more direct comparison, the fields have been extracted along two profiles along the x- and y-axis on the seafloor and plotted together with the bathymetry in Fig. 7. The field components which are supposed to be zero for the flat seafloor model cannot be expected to be exactly zero when computed by the finite element approximation. They are, however, significantly smaller than the non-vanishing components of the same and the bathymetry model (compare, for example, E_y on the x-profile). The influence of the seafloor topography is strong enough to create even a visual distinction between the flat seafloor and bathymetry fields, for example, for E_z in the x-profile and for H_y in the y-profile. Even more pronounced is the effect on the field components which vanish for the flat seafloor model, that is, H_x, E_y and H_z in the x-directed profile and H_x, E_y and E_z in the y-directed profile.

3.3 Disc models

Our third numerical example is a variation on the canonical disc model proposed by Weiss & Constable (2006). The canonical disc model (Fig. 8a) comprises a disc centred 1 km beneath the interface of a two-layered background. The two halfspaces represent seawater (3.3 S m^{-1}) and sediments (1 S m^{-1}). The disc is regarded as the simplified model of a hydrocarbon reservoir. Its parameters are 2 km radius, 100 m height and 0.01 S m^{-1} conductivity. We consider four variants (compare Fig. 8 and Table 2): (i) the canonical disc model without disc; (ii) the canonical disc model itself; (iii) and (iv) are derived from variants (i) and (ii) by replacing the water halfspace by a finite, 1 km thick water layer and an air halfspace (10^{-8} S m^{-1}). Note that variants (i) and (iii) are 1-D models which allow the comparison of our numerical results with the analytic solution.

In all cases, the transmitter, an x-directed, horizontal electric dipole operating at a frequency of 1 Hz, is placed 100 m above the seafloor and 1 km off the edge of the disc. We measure all electric and magnetic field components along an inline profile running directly across the centre of the disc. Therefore, the components H_x, E_y and H_z are expected to vanish for symmetry reasons.

The computational domain for cases (i) and (ii) without air halfspace has been chosen according to Weiss & Constable (2006) to compare our results with those of C. Weiss's finite volume code FDM3D. For the variants (iii) and (iv) including the air halfspace we had to enlarge the computational domain considerably from 11 km × 11 km × 4.5 km to 66 km × 66 km × 66 km to capture the effect of the air halfspace well enough for a transmitter/receiver distance of up to 8.5 km. We note that this result is largely influenced by our simple choice of a fullspace background model for the primary field. An air/seawater background model is expected to give satisfactory results for a smaller computational domain. However, we prefer the fast evaluation of a fullspace solution to the computationally much more elaborate evaluation of a layered earth solution. Note that, to compute the integrals defining the right hand side [eq. (4c)], the primary field has to be evaluated at least once for every element whose conductivity deviates from the background conductivity. The drawback of a larger computational domain is alleviated by the fact that our unstructured tetrahedral mesh easily permits both increasing the element size towards the boundary and retaining well-shaped elements.

As in the previous examples, we generate a coarse initial mesh, perform some steps of adaptive mesh refinement using a piecewise linear finite element approximation and compute a piecewise quadratic finite element solution only on the finest mesh level. For the model variants without air, five steps of mesh refinement produce a mesh of roughly 106 000 elements which amounts to about 675 000 dofs (Table 2). Since the starting mesh for the air halfspace variants is larger, only two steps of mesh refinement lead to comparable numbers, about 114 000 elements and 735 000 dofs. Interestingly enough, the two different model sizes and mesh refinement processes lead to a system matrix $\boldsymbol{A}$ which has a larger elimination graph for the smaller problem with fewer dofs than for

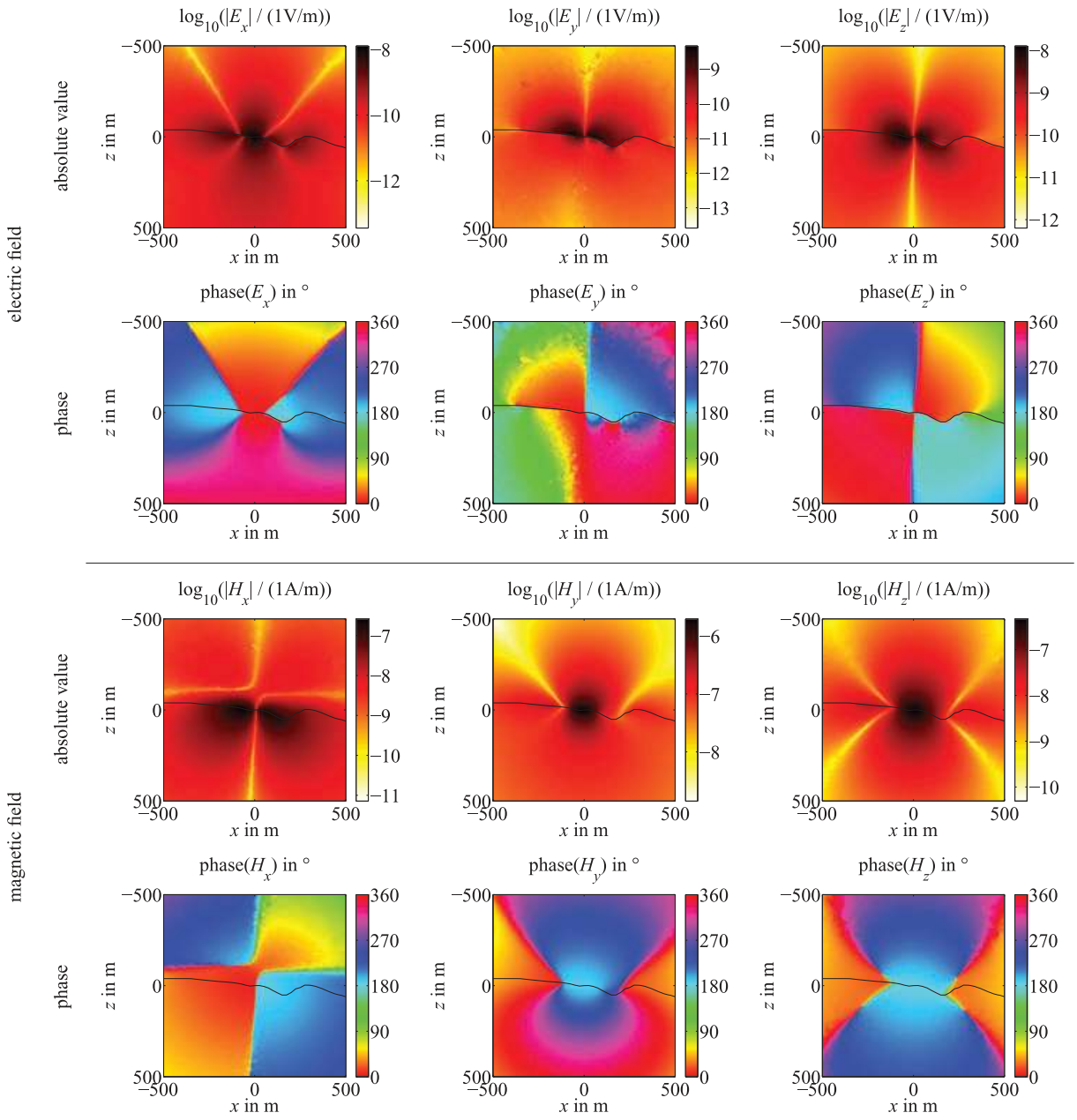

Figure 6. Bathymetry model. Secondary electric (top panel) and magnetic (bottom panel) field components in the x–z plane at $y = 0$. Absolute value and phase of the complex vector components.

the larger problem with more dofs. This can be seen from the solution times and memory consumption given in Table 2. The longer run times for the first two models are not so much caused by the three additional steps of mesh refinement and the computations involved therein but rather by the factorization of the system matrix during the production run. While the LU-factors of the first two cases have 589 213 481 and 604 677 393 non-zeros, the LU-factors of the air halfspace model system matrices only have 425 646 282 non-zeros.

The non-vanishing field components E_x, H_y and E_z of our finite element solution are plotted in Fig. 9. The fields for the four different disc model variants are indistinguishable for a transmitter/receiver distance $|x| < 2.5$ km. At $x \approx 2.5$ km the fields for the model variants with disc start to split from those without disc. The fields decay slower if the resistive disc is present. The presence of the air halfspace is only detected in the horizontal field components. For the models without disc, the influence of the air halfspace is visible for $x > 4.5$ km, and for $x > 6.5$ km for the models with disc. The numerical approximation of the vertical electric field of the disc model with air halfspace incorrectly changes sign at $x \approx 7.7$ km. Here, we reach the limit of accuracy for the present mesh size and polynomial degree. Discretization errors caused by the highly non-uniform mesh, which is rather coarse at large distances from the source, become significant for E_z at $x > 7$ km.

The fields of the model variants without air halfspace also show an artefact at $x > 8$ km. This part of the profile is less than 500 m apart from the boundary of the computational domain where the tangential field components are forced to vanish. The numerical solution shown in Fig. 9 consequently takes a sharp turn toward zero.

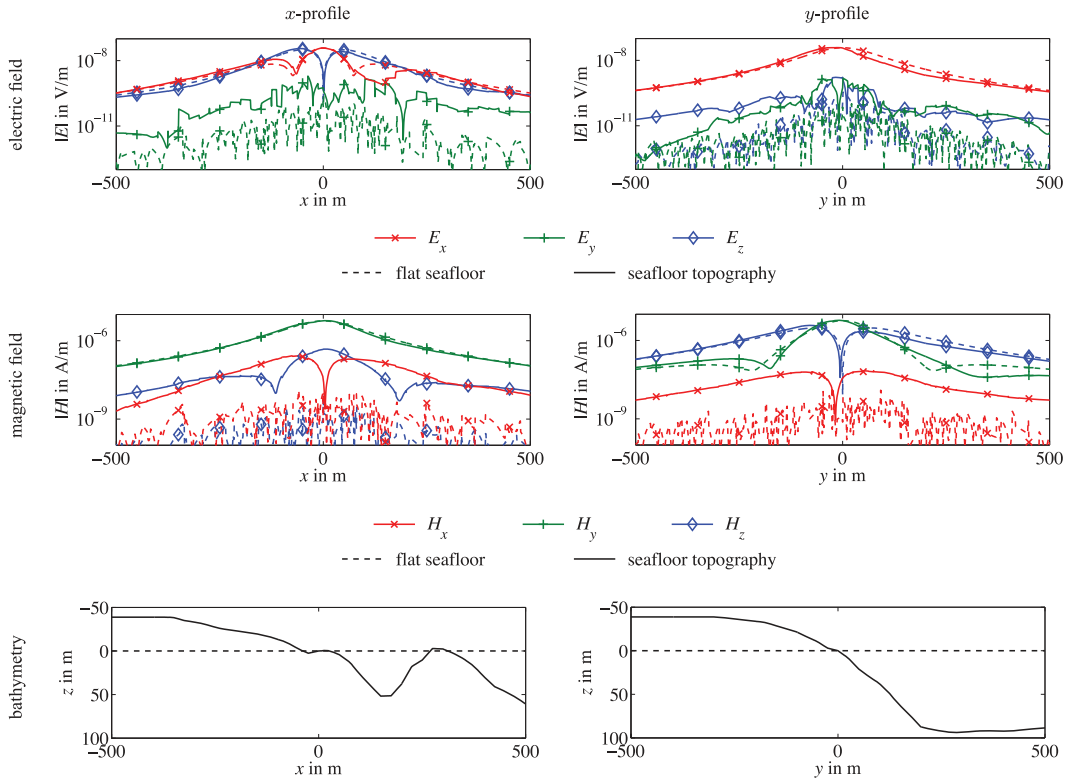

Figure 7. Bathymetry model. Absolute value of the secondary electric field (top panel) and magnetic field (middle panel) along an x-directed profile at $y = 0$ (left-hand side) and along a y-directed profile at $x = 0$ (right-hand side) recorded on the seafloor. Bottom panel: seafloor bathymetry of the profile.

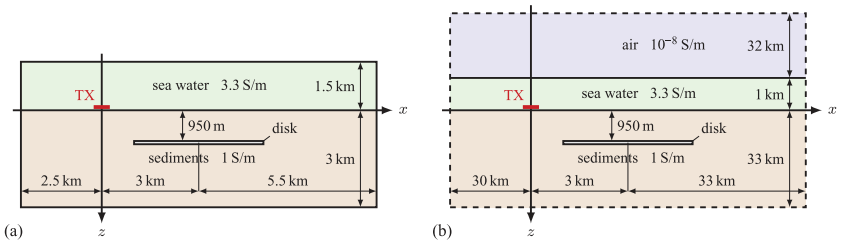

Figure 8. (a) Plan view of the canonical disc model by Weiss & Constable (2006). (b) Our extension by an air halfspace. The disc has a radius of 2 km, a height of 100 m and a conductivity of 0.01 S m^{-1}. The layers extend in y-direction perpendicularly to the drawing plane to ±5.5 km (a) and ±33 km (b). Note that only part of the computational domain is shown in case (b). The x-directed electric dipole (TX) is placed 100 m above the seafloor and operates at a frequency of 1 Hz.

Table 2. Disc model variants and their statistics: number of mesh levels, number of elements and degrees of freedom (dofs) of the final mesh with piecewise quadratic basis functions ($p = 2$), system matrix 1-norm condition number $\kappa(\boldsymbol{A})$, run time including the mesh refinement, and peak virtual memory consumption. We also list the statistics of the finite volume (FV) solution for the canonical disc model (FDM3D, Weiss & Constable 2006) which is used as a reference solution.

Model variant	Mesh levels	Elements	dofs	$\kappa(\boldsymbol{A})$	Time	Memory
Water/sediments	6	106 020	672 878	6.7×10^6	747 s	11.7 GB
Water/sediments+disc	6	106 440	675 544	1.1×10^7	773 s	12.0 GB
Air/water/sediments	3	114 608	733 396	5.1×10^{11}	400 s	9.0 GB
Air/water/sediments+disc	3	114 608	733 396	5.1×10^{11}	396 s	9.0 GB
Water/sediments+disc, FV	N/A	1 536 000	4 518 780	N/A	547 s	0.9 GB

This effect can be seen more clearly when the numerical solution is normalized by the analytic solution for a layered earth as shown in Fig. 10. The normalization coalesces the graphs of the two models without disc. Logarithmised absolute values of 0 and phases of 0 indicate the high quality of our numerical solution. Only the vertical electric field E_z shows significant errors at $x > 7$ km, as discussed previously. The normalization also very nicely isolates the effect of the resistive disc. The presence of the air halfspace, however, masks

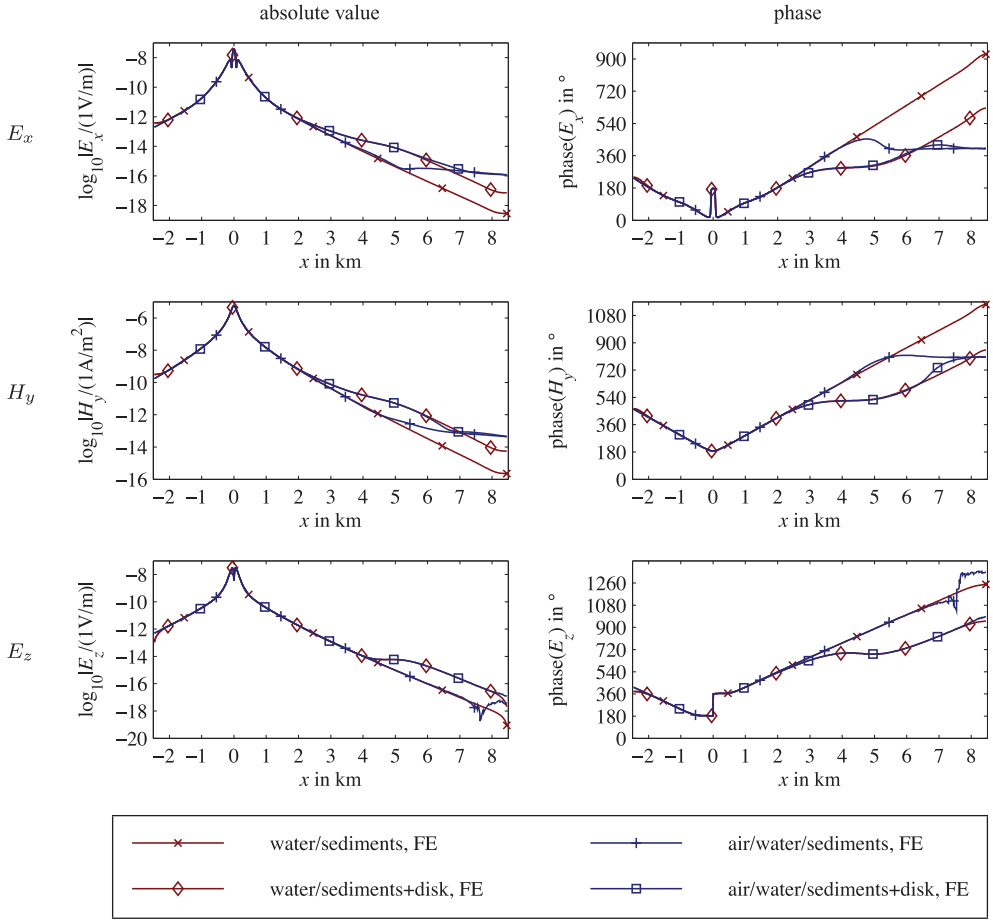

Figure 9. Finite element (FE) solution for four disc model variants. Non-vanishing in-line field components along a profile across the centre of the disc at $x = 3$ km.

this effect such that fields for the air halfspace model variants with and without disc can hardly be distinguished for $x > 7$ km.

Fig. 10 additionally gives a numerical solution for the canonical disc model obtained from C. Weiss's finite volume (FV) code FDM3D which should be compared to the finite element solution labelled 'water/sediments+disc, FE'. Both numerical solutions show a very good agreement for $|x| > 1.5$ km. Due to identical computational domains, they suffer from the same problem with artifical boundary conditions. The major difference lies in the vicinity of the source where our adaptive, unstructured tetrahedral mesh gives superior results. While the finite element mesh is locally refined around $x = 0$ on the seafloor such that the smallest edge length is about 6.9 m, the tensor product grid for the finite volume solution is not especially adapted to the solution and has a 10 times larger smallest edge length. This difference in mesh size as well as the only piecewise linear approximation account for the larger errors of the finite volume solution around the source.

The fundamental differences between the two approaches, finite volume method, piecewise linear approximation, tensor product grid, iterative solver (QMR) on the one hand and finite element method, piecewise quadratic approximation, adaptive unstructured tetrahedral mesh, direct solver on the other hand, are also reflected by the numbers given in the second and fifth line of Table 2. Despite the eight times larger number of unknowns, the matrix free implementation and the iterative solver of FDM3D clearly outperform our code in terms of memory consumption. At first sight, the run time is comparable. However, we have to mention that the direct solver PARDISO in our finite element code made use of four parallel threads while FDM3D only ran on one thread.

4 CONCLUSIONS

This paper's numerical experiments provide a proof-of-principle for our new vector finite element code. Our software allows for complex geometries as demonstrated by a marine CSEM example model featuring seafloor topography. Bathymetric data can easily be included into the simulation by solving the underlying boundary problem by the finite element method on unstructured tetrahedral meshes. Adaptive mesh refinement tailors the mesh to a particular solution and reduces the solution error to an acceptable level of a few per cent. The primary/secondary field approach restricts the numerical approximation to the secondary field and enhances the accuracy of the total field compared to a straightforward total field approach. The use of a higher order polynomial finite element approximation proved to be beneficial for the simple problems considered here. The benefit for more complex parameter distributions still needs to be corroborated. We encourage the use of second-order polynomials which provide a good balance between mesh size, improved accuracy and number of unknowns.

The bathymetry model shows that seafloor topography produces a significant 3-D effect on the electric and the magnetic field on the seafloor. When real-world marine CSEM measurements are to be simulated and interpreted, 3-D simulation software capable of

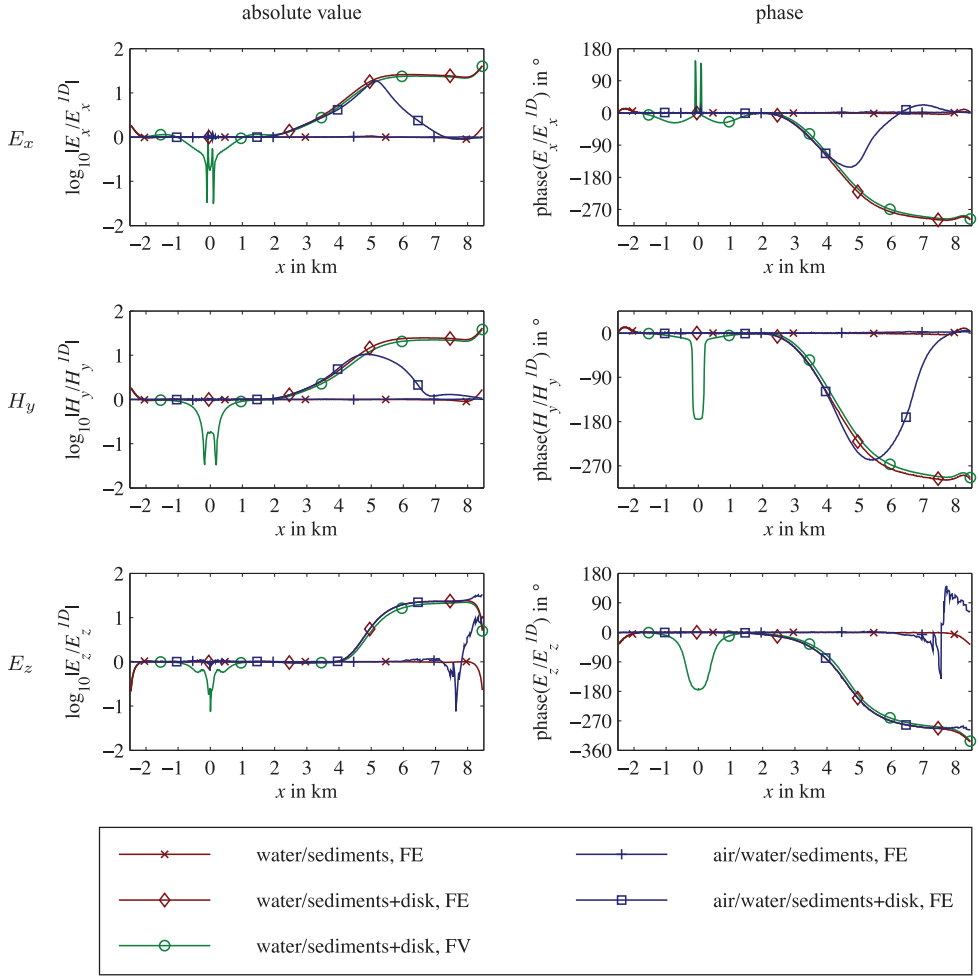

Figure 10. Finite element (FE) solution for four disc model variants and finite volume (FV) solution for the canonical disc model. Normalized, non-vanishing in-line field components along a profile across the centre of the disc at $x = 3$ km.

incorporating the bathymetry should be used to avoid artefacts and their misinterpretation.

Incorporation of an air domain into a marine CSEM scenario is challenging for at least two reasons. Firstly, the large contrast in conductivity between seawater and air and the resulting jump of the vertical electric field by orders of magnitude cause difficulties for any discretization method. Secondly, at the low frequency considered here, solutions to the boundary value problem as posed by eq. (1) can become instable if the model incorporates air. The instability is caused by the large nullspace of the curl operator as the other term $i\omega(\sigma - i\omega\varepsilon)\boldsymbol{E}_s$ becomes negligible in air. This instability is reflected in the matrix condition number of the finite element system matrix (Schwarzbach 2009). Even though the condition number was large (Table 2), considerably larger for the numerical examples including air than for the examples without air, the sparse direct solver was able to solve the system of linear equations adequately. A physically meaningful solution could be found in this case but a note of caution seems advisable when similar high-contrast scenarios and low frequencies are to be considered.

ACKNOWLEDGMENTS

C. Schwarzbach likes to thank the Studienstiftung des deutschen Volkes for financial support. K. Spitzer gratefully acknowledges financial support by the German Research Foundation DFG for the flanking numerical research projects Spi 356/9-1 and 2.

REFERENCES

Anderson, W.L., 1989. A hybrid fast Hankel transform algorithm for electromagnetic modeling, *Geophysics,* **54**(2), 263–266.

Avdeev, D.B., 2005. Three-dimensional electromagnetic modelling and inversion from theory to application, *Surv. Geophys.,* **26**(6), 767–799.

Avdeev, D.B., Kuvshinov, A.V., Pankratov, O.V. & Newman, G.A., 1997. High-performance three-dimensional electromagnetic modelling using Neumann series. Wide band numerical solution and examples, *J. Geomagn. Geoelectr.,* **49**(11-12), 1519–1539.

Badea, E.A., Everett, M.E., Newman, G.A. & Biro, O., 2001. Finite-element analysis of controlled-source electromagnetic induction using Coulomb-gauged potentials, *Geophysics,* **66**(3), 786–799.

Beck, R. & Hiptmair, R., 1999. Multilevel solution of the time-harmonic Maxwell's equations based on edge elements, *Int. J. Numer. Meth. Eng.,* **45,** 901–920.

Berenger, J.P., 1994. A perfectly matched layer for the absorption of electromagnetic waves, *J. Comput. Phys.,* **114**(2), 185–200.

Börner, R.-U., 2010. Numerical modelling in geo-electromagnetics: advances and challenges, *Surv. Geophys.,* **31**(2), 225–245.

Börner, R.-U., Ernst, O.G. & Spitzer, K., 2008. Fast 3D simulation of transient electromagnetic fields by model reduction in the frequency domain using Krylov subspace projection, *Geophys. J Int.,* **173**(3), 766–780.

Castillo, P., Rieben, R. & White, D., 2005. FEMSTER: an object oriented class library of high-order discrete differential forms, *ACM T. Math. Softw.*, **31**(4), 425–457.

Constable, S. & Weiss, C.J., 2006. Mapping thin resistors and hydrocarbons with marine EM methods: insights from 1D modeling, *Geophysics,* **71**(2), G43–G51.

Freund, R.W. & Nachtigal, N.M., 1994. An implementation of the QMR method based on coupled two-term recurrences, *SIAM J. Sci. Comput.,* **15**(2), 313–337.

Haber, E. & Ascher, U.M., 2001. Fast finite volume simulation of 3D electromagnetic problems with highly discontinuous coefficients, *SIAM J. Sci. Comput.,* **22**(6), 1943–1961.

Haber, E. & Heldmann, S., 2007. An octree multigrid method for quasi-static Maxwell's equations with highly discontinuous coefficients, *J. Comput. Phys.,* **223**(2), 783–796.

Haber, E., Ascher, U.M., Aruliah, D.A. & Oldenburg, D.W., 2000. Fast simulation of 3D electromagnetic problems using potentials, *J. Comput. Phys.,* **163**(1), 150–171.

Hohmann, G.W., 1975. Three-dimensional induced polarization and electromagnetic modeling, *Geophysics,* **40**(2), 309–324.

INRIA Gamma team, 2008. mmal25pm from 3D meshes research database, http://www-roc.inria.fr/gamma/download/affichage.php?dir=RELIEF&name=mmal25pm.

Jin, J., 1993. *The Finite Element Method in Electromagnetics,* John Wiley & Sons, New York, NY.

Mackie, R.L., Madden, T.R. & Wannamaker, P.E., 1993. Three-dimensional magnetotelluric modeling using difference equations – Theory and comparisons to integral equation solutions, *Geophysics,* **58**(2), 215–226.

Mitsuhata, Y. & Uchida, T., 2004. 3D magnetotelluric modeling using the **T**-Ω finite-element method, *Geophysics,* **69**(1), 108–119.

Mogi, T., 1996. Three-dimensional modeling of magnetotelluric data using finite element method, *J. appl. Geophys.,* **35**(2-3), 185–189.

Monk, P., 2003. *Finite Element Methods for Maxwell's Equations,* Oxford University Press, New York, NY.

Nam, M.J., Kim, H.J., Song, Y., Lee, T.J., Son, J.-S. & Suh, J.H., 2007. 3D magnetotelluric modelling including surface topography, *Geophys. Prospect.,* **55**(2), 277–287.

Nédélec, J.-C., 1980. Mixed finite elements in $\mathbb{R}^3$, *Numer. Math.,* **35**(3), 315–341.

Nédélec, J.-C., 1986. A new family of mixed finite elements in $\mathbb{R}^3$, *Numer. Math.,* **50**(1), 57–81.

Newman, G.A. & Alumbaugh, D.L., 1995. Frequency-domain modelling of airborne electromagnetic responses using staggered finite differences, *Geophys. Prospect.,* **43**(8), l021–1042.

Newman, G.A., Hohmann, G.W. & Anderson, W.L., 1986. Transient electromagnetic response of a three-dimensional body in a layered earth, *Geophysics,* **51**(8), 1608–1627.

Raiche, A.P., 1974. An integral equation approach to three-dimensional modelling, *Geophys. J. R. astr. Soc.,* **36**(2), 363–376.

Schenk, O. & Gärtner, K., 2004. Solving unsymmetric sparse systems of linear equations with PARDISO, *Future Gener. Comp. Sy.,* **20**(3), 475–487.

Schenk, O. & Gärtner, K., 2006. On fast factorization pivoting methods for symmetric indefinite systems, *Electr. Trans. Num. Anal.,* **23,** 158–179.

Schwarzbach, C., 2009. Stability of finite element solutions to Maxwell's equations in frequency domain, *PhD thesis*, TU Bergakademie Freiberg (http://nbn-resolving.de/urn:nbn:de:bsz:105-24780).

Si, H., 2007. TetGen: a quality tetrahedral mesh generator and 3D Delaunay triangulator, http://tetgen.berlios.de.

Smith, J.T., 1996. Conservative modeling of 3-D electromagnetic fields, *Geophysics,* **61**(5), 1308–1324.

Sommerfeld, A., 1964. *Vorlesungen über Theoretische Physik. Band III: Elektrodynamik,* 4th edn, Akademische Verlagsgesellschaft Geest & Portig K.-G., Leipzig.

Streich, R., 2009. 3D finite-difference frequency-domain modeling of controlled-source electromagnetic data: direct solution and optimization for high accuracy, *Geophysics,* **74**(5), F95–F105.

Wannamaker, P.E., 1991. Advances in 3D magnetotelluric modelling using integral equations, *Geophysics,* **56**(11), 1716–1728.

Wannamaker, P.E., Hohmann, G.W. & SanFilipo, W.A., 1984. Electromagnetic modeling of three-dimensional bodies in layered earths using integral equations, *Geophysics,* **49**(1), 60–74.

Weidelt, P., 1975. Electromagnetic induction in three-dimensional structures, *Geophys. J. R. astr. Soc.,* **41**(1), 85–109.

Weidelt, P., 2007. Guided waves in marine CSEM, *Geophys. J Int.,* **171**(1), 153–176.

Weiss, C.J. & Constable, S., 2006. Mapping thin resistors and hydrocarbons with marine EM methods, Part II – Modeling and analysis in 3D, *Geophysics,* **71**(6), G321–G332.

Xiong, Z. & Tripp, A.C., 1997. 3-D electromagnetic modeling for near-surface targets using integral equations, *Geophysics,* **62**(4), 1097–1106.

Zunoubi, M.R., Jin, J.-M., Donepudi, K.C. & Chew, W.C., 1999. A spectral Lanczos decomposition method for solving 3-D low-frequency electromagnetic diffusion by the finite-element method, *IEEE Trans. Antennas Propag.,* **47**(2), 242–248.

Zyserman, F.I. & Santos, J.E., 2000. Parallel finite element algorithm with domain decomposition for three-dimensional magnetotelluric modelling, *J. appl. Geophys.,* **44**(4), 337–351.